

## Research article

Qiong He, Fei Zhang, MingBo Pu, XiaoLiang Ma, Xiong Li, JinJin Jin, YingHui Guo and XianGang Luo\*

# Monolithic metasurface spatial differentiator enabled by asymmetric photonic spin-orbit interactions

<https://doi.org/10.1515/nanoph-2020-0366>

Received July 3, 2020; accepted August 22, 2020; published online September 15, 2020

**Abstract:** Spatial differentiator is the key element for edge detection, which is indispensable in image processing, computer vision involving image recognition, image restoration, image compression, and so on. Spatial differentiators based on metasurfaces are simpler and more compact compared with traditional bulky optical analog differentiators. However, most of them still rely on complex optical systems, leading to the degraded compactness and efficiency of the edge detection systems. To further reduce the complexity of the edge detection system, a monolithic metasurface spatial differentiator is demonstrated based on asymmetric photonic spin-orbit interactions. Edge detection can be accomplished via such a monolithic metasurface using the polarization degree. Experimental results show that the designed monolithic spatial differentiator works in a broadband range. Moreover, 2D edge detection is experimentally demonstrated by the proposed monolithic metasurface. The proposed design can be applied at visible and near-infrared wavelengths by proper

dielectric materials and designs. We envision this approach may find potential applications in optical analog computing on compact optical platforms.

**Keywords:** asymmetric photonic spin-orbit interactions; edge detection; metasurface; spatial differentiator.

## 1 Introduction

Edge detection captures the edge information and provides the most significant outlines of an image or an object, which has been widely applied in image processing and computer vision owing to the high processing speed and low data volume [1–4]. The most important process for edge detection is differentiation, a process generally operated by a spatial differentiator, either in a digital computation or an analog computation way [5–7]. Compared with digital computing, optical analog computing can process parallel information with high efficient and low power consumption, holding great potential in real-time detections [8–11]. However, in the traditional optical computing system, a 4-F optical system containing at least two lenses and a spatial filter is required for Fourier transform and inverse Fourier transform, which is bulky and complicated, hindering the applications in modern optoelectronics with high integration level.

Metasurfaces [12–15], single or few-layer sub-wavelength structures which are capable of modulating the phase, amplitude, and polarization of electromagnetic waves [16–19], have provided new strategies for various optical elements and systems including flat lenses [20–22], holograms [23–25], electromagnetic stealth [26–28], vortex beam generator [29], tunable optical components [30, 31], flat displays [32, 33], and so on. Notably, optical spatial computing based on metamaterials including differentiators, integrators, and equation solvers is proposed by Silva et al in 2014 [34], opening new avenues for optical analog computing. Since then, various differentiator metasurfaces are developed based on photonic crystals [5, 35],

**Qiong He and Fei Zhang:** These authors contributed equally to this work.

\***Corresponding author: XianGang Luo**, State Key Laboratory of Optical Technologies on Nano-Fabrication and Micro-Engineering, Institute of Optics and Electronics Chinese Academy of Sciences, Chengdu, 610209, China; and School of Optoelectronics, University of Chinese Academy of Sciences, Beijing, 100049, China, E-mail: [lxg@ioe.ac.cn](mailto:lxg@ioe.ac.cn). <https://orcid.org/0000-0002-1401-1670>

**Qiong He, Fei Zhang and JinJin Jin**, State Key Laboratory of Optical Technologies on Nano-Fabrication and Micro-Engineering, Institute of Optics and Electronics Chinese Academy of Sciences, Chengdu, 610209, China

**MingBo Pu, XiaoLiang Ma, Xiong Li and YingHui Guo**, State Key Laboratory of Optical Technologies on Nano-Fabrication and Micro-Engineering, Institute of Optics and Electronics Chinese Academy of Sciences, Chengdu, 610209, China; and School of Optoelectronics, University of Chinese Academy of Sciences, Beijing, 100049, China

spin Hall effect [36], surfaces plasmons [37], high-contrast gratings [8], and Pancharatnam-Berry (PB) phase [38, 39]. However, additional prisms or lenses are still required for plasmon coupling or Fourier transform in those applications [37, 40], which is incompatible with the flat and compact optical systems. Besides, many metasurface spatial differentiators work only in 1D edge detection [8, 9, 35, 36], restricting the practical applications in image recognition and processing.

To achieve a monolithic metasurface for spatial differentiation, the focusing and differentiation abilities should be integrated into one metasurface, which can be realized by asymmetric photonic spin-orbit interactions (PSOIs) of light. Here, we propose a monolithic metasurface spatial differentiator for edge detection without any additional lenses. Spin-dependent PB phase and spin-independent propagation phase are merged to arbitrarily and independently manipulate wavefronts of two converted spins, leading to asymmetric PSOIs of light [41, 42]. It is demonstrated that the monolithic metasurface is capable of forming both left-handed circularly polarized (LCP) and right-handed circularly polarized (RCP) images when illuminated by a linear polarized (LP) light and the edge image is acquired by using an orthogonal linear polarizer. The independent manipulation on LCP and RCP lights of the proposed monolithic metasurface enables edge detection without the 4F system, leading to edge detection systems with higher integration level and compactness. Four samples (three for 1D differentiation with different edge resolutions and one for 2D differentiation) are fabricated to demonstrate the tunable resolution at different orientations and 2D edge detection, respectively. The monolithic metasurface spatial differentiator works at a broadband with an edge resolution of about  $49.4\ \mu\text{m}$ . Notably, by integrating the linear polarizer into the metasurface, the overall compactness

can be further improved. This work is helpful for the applications of monolithic metasurface in edge detection and the multifunctionality of other monolithic metasurfaces based on PSOIs.

## 2 Theoretical analyses

The principle of the monolithic metasurface spatial differentiator is based on asymmetric PSOIs, as shown in Figure 1. When the LP light illuminates on the object and passes through the metasurface, the LCP and RCP images are formed at different positions with a slight distance due to the independent manipulation on the wavefronts of both LCP and RCP light. By inserting a linear polarizer, the overlapped LP light is eliminated, leaving the edge image. It is worth noting that traditional metasurfaces edge detection performs differentiation operations in the spatial Fourier domain by using the 4-F optical system, while the metasurface in this manuscript can manipulate the image directly, enabling a monolithic metasurface spatial differentiator.

For simplicity, we first analyze the mechanism of 1D edge imaging. Under the illumination of the LP light along the  $x$ -axis, the proposed metasurface can project two images of the object with a transverse shift of  $\pm\Delta$ , corresponding to LCP and RCP images, respectively. Thus, the image can be expressed as

$$E_{\text{image}}(x, y) = E_0[(x - \Delta), y] \begin{bmatrix} 1 \\ -i \end{bmatrix} + E_0[(x + \Delta), y] \begin{bmatrix} 1 \\ i \end{bmatrix} \quad (1)$$

When  $\Delta$  is far smaller than the imaging distance, the phase difference between the LCP and RCP components at the same point can be ignored. As a result, the overlapped area of the

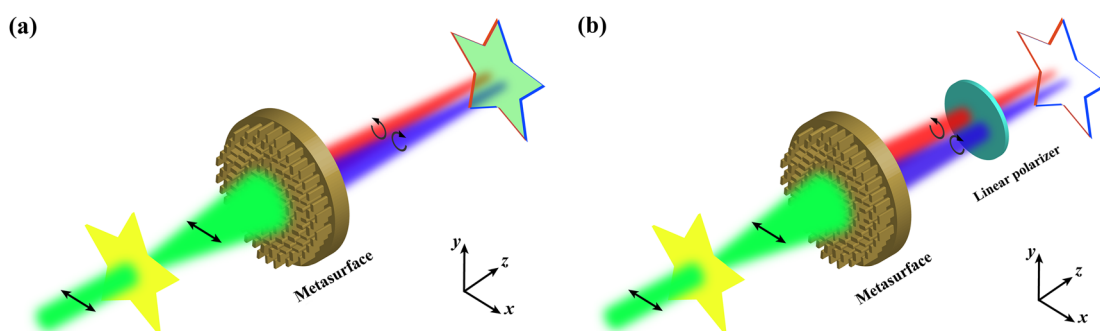


**Figure 1:** Schematic of the proposed monolithic metasurface.

(a) The monolithic metasurface for left-handed circularly polarized (LCP) and right-handed circularly polarized (RCP) imaging with an opposite shift along the phase gradient direction ( $x$ -axis in this figure). (b) A linear polarizer is applied to eliminate the LP image of the overlapped LCP and RCP images for edge detection.

LCP and RCP images retains the original incident polarization state and thus can be filtered with an orthogonal linear polarizer. Then, the final edge can be expressed as [38]

$$E_{\text{edge}}(x, y) = \{E_0[(x + \Delta), y] - E_0[(x - \Delta), y]\} \begin{bmatrix} 0 \\ i \end{bmatrix} \quad (2)$$

If the  $\Delta$  is small enough, the edge information along the  $x$ -axis is recorded, which is tunable by adjusting the shift distances between LCP and RCP images. This description suggests that the proposed metasurface can generate two different phase distributions for LCP and RCP light. In accordance with the aforementioned analysis, the two-phase distribution can be written as

$$\begin{aligned} \phi_\sigma(x, y) &= -k_0 \sqrt{x^2 + y^2 + f^2} + k_\sigma x \\ k_\sigma &= \sigma k_0 \sin \zeta \end{aligned} \quad (3)$$

where  $f$  is the focal length;  $k_0 = 2\pi/\lambda$  is the wavenumber in free space;  $\sigma = \pm 1$  indicates RCP and LCP light;  $k_\sigma$  corresponds to the additional horizontal momentum [43],  $\zeta$  determines the degree of separation between LCP and RCP images. When  $\zeta$  is small enough, the shift value  $\Delta$  along the  $x$ -axis can be approximately equal to  $\zeta v$ , where  $v$  indicates the imaging distance and  $\zeta$  should be converted to radians. Thus, the edge width depends on the separation and the resolution of the obtained edge images is limited by the diffraction limit of the designed metasurface due to the nearly perfect focusing phase distribution as indicated by Eq. (3). For 2D edge detection, the aforementioned phase distribution should be modified as

$$\phi_\sigma(x, y) = -k_0 \sqrt{x^2 + y^2 + f^2} + k_\sigma \sqrt{x^2 + y^2} \quad (4)$$

The independent control of LCP and RCP light is the key for edge detection with a monolithic device, which can be realized by asymmetric PSOs. For simplicity, assuming a lossless anisotropic subwavelength structure with the phase shift of  $\beta \pm \delta/2$  along its major and minor axes, the Jones matrix can be described as  $\text{diag}[\exp(i\beta + i\delta/2), \exp(i\beta - i\delta/2)]$ . After being rotated by  $\theta$  along the optical axis and under the normal illumination of circularly polarized (CP) light of  $[1 - i\sigma]^T$ , the output optical field can be given as [41, 44]

$$\cos \frac{\delta}{2} e^{i\beta} \begin{bmatrix} 1 \\ -i\sigma \end{bmatrix} - i \sin \frac{\delta}{2} e^{i(-2\sigma\theta + \beta)} \begin{bmatrix} 1 \\ i\sigma \end{bmatrix} \quad (5)$$

From the Eq. (5), the flipped spin component carries not only spin-independent propagation phase  $\beta$  but also spin-dependent PB phase  $-2\sigma\theta$ . The propagation phase can break the conjugation symmetry of optical fields generated by PB-based metasurfaces, leading to asymmetric PSOs. Such two phases can be independently controlled by

changing the size and orientation of the subwavelength structure, respectively. Then, the propagation phase and orientation at the coordinate  $(x, y)$  can be given as

$$\beta(x, y) = \frac{1}{2} [\phi_1(x, y) + \phi_{-1}(x, y)] \quad (6)$$

$$\theta(x, y) = \frac{1}{4} [\phi_{-1}(x, y) - \phi_1(x, y)] \quad (7)$$

where  $\phi_1(x, y)$  and  $\phi_{-1}(x, y)$  are independent phase distributions for  $\sigma = \pm 1$ .

### 3 Simulation and sample fabrication

As a proof-of-concept demonstration, a metasurface spatial differentiator that works at  $10.6 \mu\text{m}$  has been designed and fabricated. The unit cell is a chamfered pillar on the substrate and silicon is chosen as the dielectric material because of the straightforward fabrication processes and negligible loss at the infrared band, as illustrated in Figure 2a. The pillars with the same height of  $H = 7 \mu\text{m}$  but different transverse sizes (width  $W$  and length  $L$ ) and orientations  $\theta$  are mounted on the hexagonal unit cells with a lattice constant of  $P$ . Because such high-contrast pillars can work as weakly coupled low-quality-factor Fabry-Pérot resonators, propagation and PB phases can be independently controlled by changing the size and orientation [45]. Eight unit cells with an incremental propagation phase of  $\sim \pi/4$  are designed at the wavelength of  $10.6 \mu\text{m}$ , with their propagation phase and transmittances shown in Figure 2b. As can be seen, a  $0-2\pi$  phase coverage, high cross-polarized transmittance, and low co-polarized transmittance are realized by these eight unit cells, which indicate that all the unit cells approximately work as a local half-wave plate, that is,  $\delta = \pi$ . In fact, the unit cells of the metasurfaces cannot behave like a perfect half-wave plate, indicating the existence of the co-polarized lights. However, the co-polarized LCP and RCP lights will not be separated and the polarization states remain unchanged, and thus, the merged light is still LP, which will be filtered by the orthogonal linear polarizer. Consequently, the remaining co-polarized transmittance lights only decrease the efficiency of the metasurface spatial differentiator and cannot contribute to the differential functionality. In accordance with Eqs. (6) and (7), four edge detectors are designed with the same diameter of  $1 \text{ cm}$  and a focal length of  $2 \text{ cm}$  working at  $10.6 \mu\text{m}$ . These four samples correspond three 1D edge detectors (denoted by S1, S2, and S3 with respective  $\zeta = 0.1, 0.075$  and  $0.05^\circ$ ) and one 2D edge detector (denoted by S4 with  $\zeta = 0.05^\circ$ ).

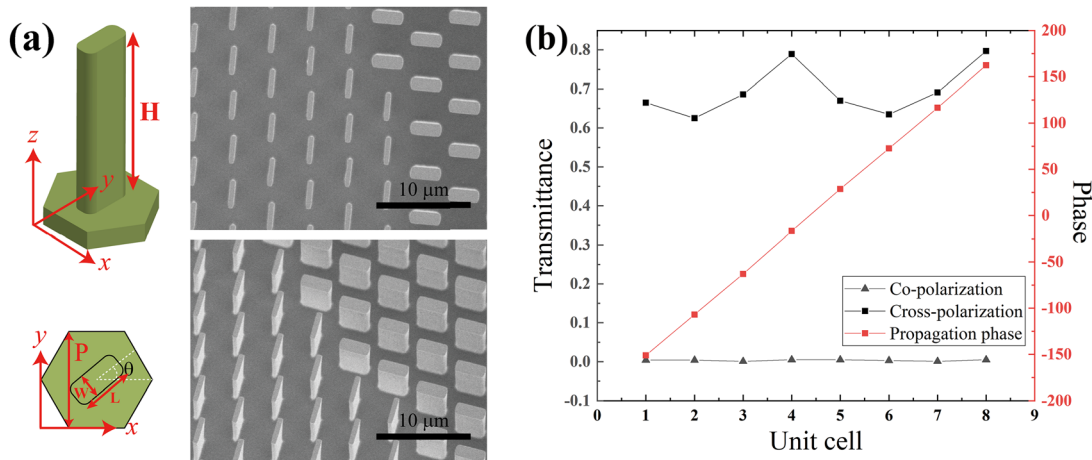


**Figure 2:** Design and simulation results of the unit cells.

(a) Schematic images of the unit cell and scanning electron microscope (SEM) images of the samples. A hexagonal shape is designed because the circular symmetry of the hexagonal shape is higher than the square, leading to more uniform responses of the unit cells at different rotation angles for Pancharatnam-Berry (PB) phase. The period  $P$  of the unit cell and the height  $H$  of the pillar are  $4.8$  and  $7\ \mu\text{m}$ , respectively. The edges of the pillar in this design are bent by a radius of  $W/4$ , where  $W$  is the width of the pillar. (b) Simulation results of eight unit cells including co-polarization, cross-polarization transmittance and propagation phase at  $10.6\ \mu\text{m}$ . The sizes of unit cells 1–4 are  $L = 3.8, 3.45, 3.1, 3.5\ \mu\text{m}$  and  $W = 1.75, 1.6, 1.43, 1\ \mu\text{m}$ , respectively. The results of unit cells 5–8 are obtained by rotating unit cells 1–4 by  $90^\circ$ .

The metasurfaces are fabricated by the laser direct writing and inductively coupled plasma (ICP) etching processes. Specifically,  $1\text{-}\mu\text{m}$  thick positive photoresist (AZ1500) was spin-coated onto the clean silicon substrates and prebaked at  $150\ ^\circ\text{C}$  for  $5\ \text{min}$ , followed by the laser direct writing and corresponding developing processes. Next, ICP etching was used to fabricate the silicon pillars where the positive photoresist acts as the mask. The fabrication processes are simple and low cost, holding great potential for the applications of such monolithic metasurface in edge detection systems. Morphologies of the samples were characterized by scanning electron microscope, as shown in the right part of Figure 2a. More photographs of the samples and spectra of the unit cells are shown in the Supplementary materials.

## 4 Results and discussion

We first demonstrate the 1D edge detection at different orientations by the experimental setup shown in Figure 3a. A  $\text{CO}_2$  laser was utilized as the light source. After passing through a linear polarizer and a  $1/4$  wave plate, the beam was sent through the object and then transmitted to the sample. The transmitted beam was filtered by another linear polarizer and recorded by an infrared detector ( $800 \times 600$  pixels with a pixel size of  $17 \times 17\ \mu\text{m}$ ) with a video capture card (TC-UB625). The 1D edge images and 2D edge images were magnified through the built-in interpolation algorithm to four and two times, respectively,

indicating the effective pixel sizes of respective  $4.25 \times 4.25\ \mu\text{m}$  and  $8.5 \times 8.5\ \mu\text{m}$  for 1D and 2D images throughout this experiment. It is worth noting that the first linear polarizer and the  $1/4$  wave plate are required just for CP imaging and the edge detection can be realized through only the metasurface and a linear polarizer. With the development of micro-/nano-fabrication, the linear polarization can be fabricated on the backside of the metasurface, further reducing the complexity and improving the integration level of the spatial differentiation system. Therefore, compared with other optical edge detection systems, our experimental setup is free of the 4F system, which means that the system volume along the optical axis can be reduced by  $50\%$ , suggesting higher integration level and compactness in practical applications.

From the first row of Figure 3b, one can see clear LCP and RCP images, indicating excellent independent control on the wavefronts of both LCP and RCP light enabled by the high-efficiency asymmetric PSOs. When the overlapped area of the LCP and RCP image is filtered by the orthogonal linear polarizer, a clear edge along the  $x$ -axis appears. Besides, the phase gradient of the metasurfaces can be designed at arbitrary directions, implying edge detection at different orientations. By rotating the metasurface, CP images and the corresponding edge images at different orientations were obtained as shown in Figure 3b. Similar to the first row of Figure 3b, LCP and RCP images for other orientations shift to opposite directions along the designed phase gradient, leaving the clear edge images. However, the fabrication error can lead

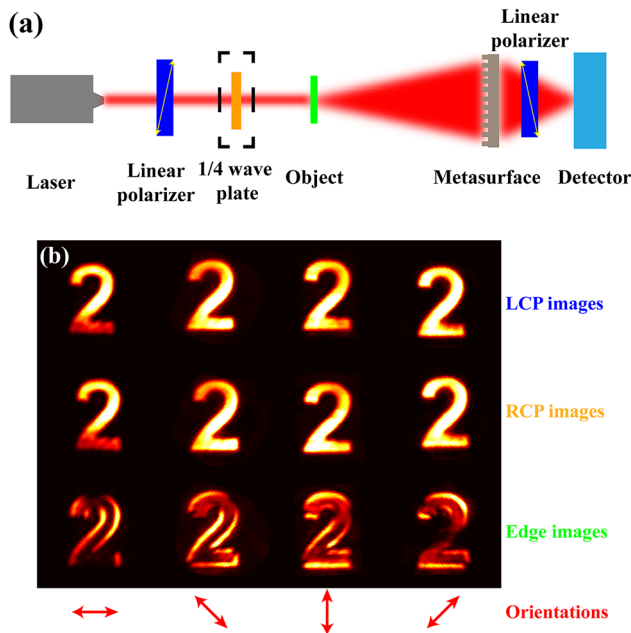


**Figure 3:** 1D edge detection setup and the corresponding images. (a) Schematic illustration of the measurement setup for edge detection. (b) LCP images, RCP images, and 1D edge images of the number ‘2’ at different orientations. The rows from top to bottom are LCP images, RCP images, and 1D edge images. The columns from left to right are images at 0, 45, 90, and 135°.

to the imbalance of intensities between LCP and RCP lights, and thus the merged light will be elliptically polarized. Consequently, the linear polarizer is not able to eliminate the overlapped light completely, leaving the inner fields in the edge images.

Then, the tunable resolution of the edge detection is further demonstrated. The edge images of S1, S2, and S3 are shown in Figure 4a–c. It is clear that when  $\zeta$  is decreased, the edge of the image turns thinner, which is attributed to the proportional relation between the edge width and the  $\zeta$ , as described by  $w = 2\Delta = 2\zeta v$ . The three samples share the same  $f$  (2.0 cm) and object distance  $u$  (6.8 cm) during the measurement, so the imaging distance  $v$  can be calculated to be 2.8 cm in accordance with the Gauss formula. Accordingly, the theoretical edge widths for S1, S2, and S3 are, respectively, 98.8, 74.1, and 49.4  $\mu\text{m}$ , which can be easily distinguished by the detector with a resolution of 34  $\mu\text{m}$ . Here, the edge widths along the x-axis of the three images are measured to be 101.6, 78.1, and 54.7  $\mu\text{m}$ , which are close to the theoretical values. In accordance with the relation between the edge width and  $\zeta$ , the edge width can be further reduced by decreasing the  $\zeta$ . However, considering that the final edge image is also constrained by the resolution of the detector, which means edge width smaller than the resolution of the detector will not be

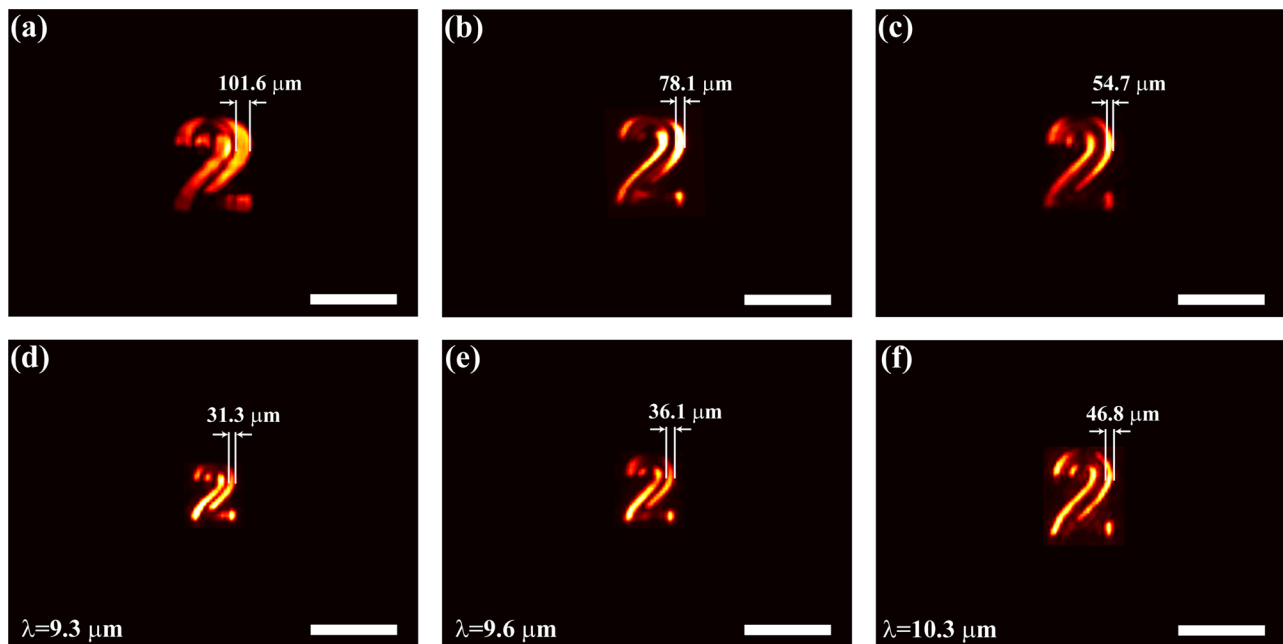


**Figure 4:** Demonstration of tunable edge resolution 1D edge detection and broadband 1D edge detection. (a), (b), and (c) 1D edge images of the number “2” by using S1, S2, and S3 at 10.6  $\mu\text{m}$ . (d), (e), and (f) Broadband 1D edge detection demonstrated by S3 at the wavelengths of 9.3, 9.6, and 10.3  $\mu\text{m}$ , respectively. The edge detection can work at broadband from 9.3 to 10.6  $\mu\text{m}$  (scale bar is 500  $\mu\text{m}$ ).



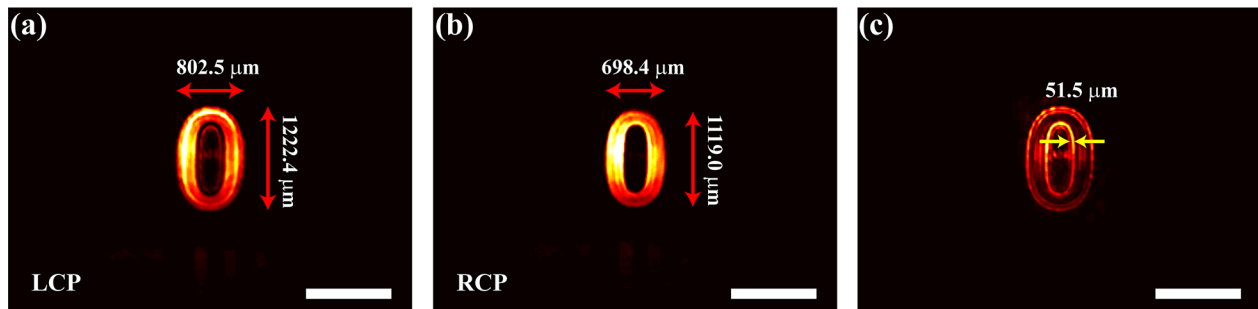


**Figure 5:** Experimental demonstration of 2D edge detection by S4.

(a) The expanded LCP image of “0”. (b) The shrunk RCP image of “0”. (c) Edge image of “0”. (Scale bar is 1000  $\mu\text{m}$ ).

distinguished, the metasurface should be carefully designed in accordance with the specific application and detector to ensure an optimal edge image.

The work bandwidth is further tested by changing the wavelength of a  $\text{CO}_2$  laser. Different from the continuous laser, the wavelength of the  $\text{CO}_2$  laser cannot be tuned to an arbitrary value, so we chose some specific wavelengths of the  $\text{CO}_2$  laser, 9.3, 9.6, and 10.3  $\mu\text{m}$  to verify the edge detection bandwidth of S3. By changing the wavelength and object distance, the corresponding edge images are obtained with fixed image distance, as shown in Figure 4d–f. The clear edge images for different wavelengths indicate that the metasurface differentiator works well from the designed working wavelength at 10.6–9.3  $\mu\text{m}$  with a slight degradation of edge image quality. Although the wavelength beyond 10.6  $\mu\text{m}$  is not measured limited by the  $\text{CO}_2$  laser, it could be inferred from the high image quality at 10.6  $\mu\text{m}$  that such differentiator can also work at wavelength beyond 10.6  $\mu\text{m}$  to a certain range, indicating a broadband (over 2.3  $\mu\text{m}$ ) working ability. Besides, one can see from Figure 4c–f that the size of the image “2” increases with the increasing working wavelength, which originates from the wavelength-dependent focal length of the metasurface. Specifically, when the wavelength is decreased, the  $f$  and the corresponding  $u$  are increased for a certain  $v$ , leading to a smaller magnification, and thus, the image size is smaller at shorter wavelength. Meanwhile, reduced magnification implies decreased equivalent  $\zeta$ , so the edge width at a shorter wavelength is thinner, as indicated by Figure 4c–f.

Finally, the 2D edge detection capability of S4 is demonstrated with the same experimental setup in Figure 3a. Figure 5 shows the LCP/RCP image and the edge image of the number “0”. The heights and widths of the “0” for LCP and RCP are, respectively, approximately 1222.4, 802.5, 1119.0, and 698.4  $\mu\text{m}$ , which results from that the LCP image expands while the RCP image shrinks along the radial direction. If the overlapped LP image is eliminated

by a linear polarizer, the 2D edge image appears, suggesting the capability of 2D edge detection of the proposed monolithic metasurface. Moreover, the edge width in Figure 5c is  $\sim 51.5 \mu\text{m}$ , which is in accordance with that of 1D edge width (Figure 4c) and the theoretical edge resolution S4. Except for the experimental demonstrations of 1D and 2D edge detection shown here, some simulation results of 2D edge detection for more complex objects are provided in the Supplementary materials, which further demonstrate the ability of edge detection for the proposed metasurface spatial differentiator.

## 5 Conclusions

In conclusion, owing to the independent manipulation on LCP and RCP lights by a monolithic metasurface, edge detection without 4F system is demonstrated, suggesting a simpler and more compact edge detection system in practical applications. The proposed monolithic metasurface spatial differentiator works at a wide bandwidth over 2.3  $\mu\text{m}$  with tunable resolutions. Besides, both 1D and 2D differentiation have been experimentally demonstrated with an edge resolution of about 49.4  $\mu\text{m}$  ( $\sim 4.7 \lambda$ ), which can be improved by decreasing the horizontal momentum carried on circularly polarized light. Notably, such a monolithic spatial differentiator can be designed to work at visible and near-infrared wavelengths, which would satisfy more possible applications. We believe that the monolithic spatial differentiation metasurface in this article can be applied in compact optical imaging systems and the asymmetric PSOs can be utilized to build more kinds of multifunctional metasurfaces.

**Acknowledgments:** The authors acknowledge the financial support by the National Natural Science Foundation of China under contract Nos. 611975210 and 61822511.

**Author contribution:** All the authors have accepted responsibility for the entire content of this submitted manuscript and approved submission.

**Research funding:** This research was supported the National Natural Science Foundation of China under contract Nos. 611975210 and 61822511.

**Conflict of interest statement:** The authors declare no conflicts of interest regarding this article.

## References

- [1] D. Ziou and S. Tabbone, "Edge detection techniques – an overview," *Pattern Recogn. Image Anal.*, vol. 8, pp. 537–559, 1998.
- [2] D. R. Solli and B. Jalali, "Analog optical computing," *Nat. Photonics*, vol. 9, pp. 704–706, 2015.
- [3] H. S. Hsu, and W. H. Tsai, "Moment-preserving edge detection and its application to image data compression," *Opt. Eng.*, vol. 32, pp. 1596–1609, 1993.
- [4] S. Fühapter, A. Jesacher, S. Bernet, and M. Ritsch-Marte, "Spiral phase contrast imaging in microscopy," *Opt. Express*, vol. 13, pp. 689–694, 2005.
- [5] Y. Zhou, H. Zheng, I. I. Kravchenko, and J. Valentine, "Flat optics for image differentiation," *Nat. Photonics*, vol. 14, pp. 316–323, 2020.
- [6] A. Pors, M. G. Nielsen, and S. I. Bozhevolnyi, "Analog computing using reflective plasmonic metasurfaces," *Nano Lett.*, vol. 15, pp. 791–797, 2015.
- [7] W. Wu, W. Jiang, J. Yang, S. Gong, and Y. Ma, "Multilayered analog optical differentiating device: performance analysis on structural parameters," *Opt. Lett.*, vol. 42, pp. 5270–5273, 2017.
- [8] Z. Dong, J. Si, X. Yu, and X. Deng, "Optical spatial differentiator based on subwavelength high-contrast gratings," *Appl. Phys. Lett.*, vol. 112, p. 181102, 2018.
- [9] Y. Zhou, W. Wu, R. Chen, W. Chen, R. Chen, and Y. Ma, "Analog optical spatial differentiators based on dielectric metasurfaces," *Adv. Opt. Mater.*, vol. 8, p. 1901523, 2019.
- [10] M. Farmahini-Farahani, J. Cheng, and H. Mosallaei, "Metasurfaces nanoantennas for light processing," *J. Opt. Soc. Am. B*, vol. 30, pp. 2365–2370, 2013.
- [11] H. Kwon, D. Sounas, A. Cordaro, A. Polman, and A. Alu, "Nonlocal metasurfaces for optical signal processing," *Phys. Rev. Lett.*, vol. 121, p. 173004, 2018.
- [12] N. Yu and F. Capasso, "Flat optics with designer metasurfaces," *Nat. Mater.*, vol. 13, pp. 139–150, 2014.
- [13] X. Luo, *Engineering Optics 2.0: A Revolution in Optical Theories, Materials, Devices and Systems*, Singapore, Springer, 2019.
- [14] A. V. Kildishev, A. Boltasseva, and V. M. Shalaev, "Planar photonics with metasurfaces," *Science*, vol. 339, p. 1232009, 2013.
- [15] X. Luo, "Principles of electromagnetic waves in metasurfaces," *Sci. China Phys. Mech.*, vol. 58, p. 594201, 2015.
- [16] F. Zhang, Q. Zeng, M. Pu, et al., "Broadband and high-efficiency accelerating beam generation by dielectric catenary metasurfaces," *Nanophotonics*, vol. 9, pp. 2829–2837, 2020.
- [17] J. P. Balthasar Mueller, N. A. Rubin, R. C. Devlin, B. Groever, and F. Capasso, "Metasurface polarization optics: independent phase control of arbitrary orthogonal states of polarization," *Phys. Rev. Lett.*, vol. 118, p. 113901, 2017.
- [18] W. T. Chen, A. Y. Zhu, and F. Capasso, "Flat optics with dispersion-engineered metasurfaces," *Nat. Rev. Mater.*, vol. 5, pp. 607–620, 2020.
- [19] J. Guo, T. Wang, B. Quan, et al., "Polarization multiplexing for double images display," *Opto-Electron. Adv.*, vol. 2, p. 180029, 2019.
- [20] M. Khorasaninejad, W. T. Chen, R. C. Devlin, J. Oh, A. Y. Zhu, and F. Capasso, "Metalenses at visible wavelengths: Diffraction-limited focusing and subwavelength resolution imaging," *Science*, vol. 352, pp. 1190–1194, 2016.
- [21] S. Wang, P. C. Wu, V. C. Su, et al., "A broadband achromatic metalens in the visible," *Nat. Nanotechnol.*, vol. 13, pp. 227–232, 2018.
- [22] K. Dou, X. Xie, M. Pu, et al., "Off-axis multi-wavelength dispersion controlling metalens for multi-color imaging," *Opto-Electron. Adv.*, vol. 3, p. 190005, 2020.
- [23] G. Zheng, H. Muhlenbernd, M. Kenney, G. Li, T. Zentgraf, and S. Zhang, "Metasurface holograms reaching 80% efficiency," *Nat. Nanotechnol.*, vol. 10, pp. 308–312, 2015.
- [24] X. Li, L. Chen, Y. Li, et al., "Multicolor 3D meta-holography by broadband plasmonic modulation," *Sci. Adv.*, vol. 2, p. e1601102, 2016.
- [25] X. Xie, K. Liu, M. Pu, et al., "All-metallic geometric metasurfaces for broadband and high-efficiency wavefront manipulation," *Nanophotonics*, vol. 9, pp. 3209–3215, 2019.
- [26] W. Cai, U. K. Chettiar, A. V. Kildishev, and V. M. Shalaev, "Optical cloaking with metamaterials," *Nat. Photonics*, vol. 1, pp. 224–227, 2007.
- [27] X. Xie, X. Li, M. Pu, et al., "Plasmonic metasurfaces for simultaneous thermal infrared invisibility and holographic illusion," *Adv. Funct. Mater.*, vol. 28, p. 14, 2018.
- [28] X. Ma, M. Pu, X. Li, Y. Guo, and X. Luo, "All-metallic wide-angle metasurfaces for multifunctional polarization manipulation," *Opto-Electron. Adv.*, vol. 2, p. 180023, 2019.
- [29] P. Genevet, N. Yu, F. Aieta, et al., "Ultra-thin plasmonic optical vortex plate based on phase discontinuities," *Appl. Phys. Lett.*, vol. 100, p. 013101, 2012.
- [30] P. C. Wu, N. Papasimakakis, and D. P. Tsai, "Self-affine graphene metasurfaces for tunable broadband absorption," *Phys. Rev. Appl.*, vol. 6, p. 044019, 2016.
- [31] Q. Wang, E. T. F. Rogers, B. Gholipour, et al., "Optically reconfigurable metasurfaces and photonic devices based on phase change materials," *Nat. Photonics*, vol. 10, pp. 60–65, 2016.
- [32] M. A. Kats, R. Blanchard, P. Genevet, and F. Capasso, "Nanometre optical coatings based on strong interference effects in highly absorbing media," *Nat. Mater.*, vol. 12, pp. 20–24, 2013.
- [33] M. A. Kats, D. Sharma, J. Lin, et al., "Ultra-thin perfect absorber employing a tunable phase change material," *Appl. Phys. Lett.*, vol. 101, p. 221101, 2012.
- [34] A. Silva, F. Monticone, G. Castaldi, V. Galdi, A. Alu, and N. Engheta, "Performing mathematical operations with metamaterials," *Science*, vol. 343, pp. 160–163, 2014.
- [35] A. Cordaro, H. Kwon, D. Sounas, A. F. Koenderink, A. Alù, and A. Polman, "High-index dielectric metasurfaces performing

- mathematical operations,” *Nano Lett.*, vol. 19, pp. 8418–8423, 2019.
- [36] T. Zhu, Y. Lou, Y. Zhou, et al., “Generalized spatial differentiation from the spin hall effect of light and its application in image processing of edge detection,” *Phys. Rev. Appl.*, vol. 11, p. 3, 2019.
- [37] T. Zhu, Y. Zhou, Y. Lou, et al., “Plasmonic computing of spatial differentiation,” *Nat. Commun.*, vol. 8, p. 15391, 2017.
- [38] J. Zhou, H. Qian, C. F. Chen, et al., “Optical edge detection based on high-efficiency dielectric metasurface,” *Proc. Natl. Acad. Sci. U. S. A.*, vol. 116, pp. 11137–11140, 2019.
- [39] J. Zhou, H. Qian, J. Zhao, et al. Two-dimensional optical spatial differentiation and high-contrast imaging. *Natl. Sci. Rev.* 2020, <https://doi.org/10.1093/nsr/nwaa176>.
- [40] P. Huo, C. Zhang, W. Zhu, et al., “Photonic spin-multiplexing metasurface for switchable spiral phase contrast imaging,” *Nano Lett.*, vol. 20, pp. 2791–2798, 2020.
- [41] F. Zhang, M. Pu, X. Li, et al., “All-dielectric metasurfaces for simultaneous giant circular asymmetric transmission and wavefront shaping based on asymmetric photonic spin-orbit interactions,” *Adv. Funct. Mater.*, vol. 27, p. 47, 2017.
- [42] F. Zhang, M. Pu, J. Luo, H. Yu, and X. Luo, “Symmetry breaking of photonic spin-orbit interactions in metasurfaces,” *Opto-Electro. Eng.*, vol. 44, pp. 319–325, 2017.
- [43] X. Luo, M. Pu, X. Li, and X. Ma, “Applications. Broadband spin hall effect of light in single nanoapertures,” *Light-Sci. Appl.*, vol. 6, p. e16276, 2017.
- [44] M. Pu, X. Li, X. Ma, et al., “Catenary optics for achromatic generation of perfect optical angular momentum,” *Sci. Adv.*, vol. 1, p. e1500396, 2015.
- [45] A. Arbabi, Y. Horie, M. Bagheri, and A. Faraon, “Dielectric metasurfaces for complete control of phase and polarization with subwavelength spatial resolution and high transmission,” *Nat. Nanotechnol.*, vol. 10, pp. 937–943, 2015.

---

**Supplementary material:** The online version of this article offers supplementary material (<https://doi.org/10.1515/nanoph-2020-0366>).